Inhomogeneity of Gated and Ungated SPECT Technetium-99m-Sestamibi Bull's-Eyes in Normal Dogs: Comparison with Thallium-201

Robert L. Eisner, Sharon E. Martin, Angel R. Leon, L. Susan Schmarkey, Marquis A. Worthy, Tsann H. Chu and Randolph E. Patterson

Carlyle Fraser Heart Center, Crawford Long Hospital of Emory University, Departments of Medicine (Cardiology), Radiology and Physiology, Emory University School of Medicine, Atlanta, Georgia

By computer simulation, we have previously hypothesized, independent of the isotope imaged, that differences in view-to-view resolution and attenuation patterns predictably cause count density distortions in SPECT images. We tested the simulation predictions for both ECG-gated and ungated SPECT ^{99m}Tc-sestamibi and SPECT ^{201}Tl myocardial perfusion images in normal dogs. In agreement with the predictions of the computer model, distortions in SPECT ^{99m}Tc-sestamibi myocardial perfusion images are virtually equivalent to SPECT ^{201}Tl, dependent on the exact SPECT acquisition orbit and markedly different for a posterior 180° acquisition arc compared to an anterior 180° acquisition arc. Furthermore, ungated and gated SPECT ^{99m}Tc-sestamibi images show similar count inhomogeneities. These results suggest that little is to be gained from a 360° acquisition with SPECT ^{99m}Tc-sestamibi, and that image distortions from gated or ungated SPECT ^{99m}Tc images with 180° orbits will be similar to those in SPECT ^{201}Tl images.

J Nucl Med 1993; 34:281–287

We developed a computer simulation of SPECT imaging to model the effects of attenuation and resolution on myocardial perfusion imaging (*1*). On the basis of resolution and attenuation effects alone, we predicted that SPECT reconstructions of myocardial perfusion images would be distorted with decreased counts at the apex and an asymmetry in septal-to-lateral wall counts. The simulations also predicted that the view-to-view variability in the number of projected cardiac counts would produce myocardial images with count density distributions dependent on the starting angle and exact 180° acquisition arc. Apart from differences due to scatter, which we did not model, we also suggested that SPECT ^{201}Tl and SPECT ^{99m}Tc myocardial perfusion images would have similar distortions because of the similarity of the ^{201}Tl and ^{99m}Tc attenuation coefficients, and of an expected small improvement in the total system resolution between ^{99m}Tc versus ^{201}Tl when the same imaging collimator was used.

Previously, we compared SPECT-labeled methoxyisobutyl isonitrile (^{99m}Tc-sestamibi) with SPECT ^{201}Tl in a canine model of adenosine-induced vasodilation and partial coronary occlusion as a test to detect coronary artery disease (*2*). Results of the study indicated that, compared to SPECT ^{201}Tl, SPECT ^{99m}Tc-sestamibi underestimated the extent and severity of transient myocardial underperfusion during adenosine-stress with moderately severe partial coronary occlusion (*2*).

The objective of this investigation was to use adenosine-stress SPECT ^{99m}Tc-sestamibi myocardial perfusion images in normal dogs to:

1. Establish SPECT ^{99m}Tc-sestamibi bull's-eye for comparison in the normal dog with SPECT ^{201}Tl.
2. Evaluate the effects of resolution and attenuation on myocardial perfusion images acquired in normal dogs with different 180° acquisition arcs.
3. Compare diastolic and systolic SPECT ^{99m}Tc-sestamibi bull's-eye images in normal dogs to evaluate the effect of systolic wall thickening and cardiac motion on the regional variation of SPECT reconstructed count density.
4. Determine (apart from the technical effects of the imaging process) if there was a relationship between the inhomogeneity in SPECT ^{99m}Tc-sestamibi reconstructed counts and variations in actual left ventricular wall thickness.

METHODS

SPECT ^{99m}Tc-Sestamibi versus SPECT ^{201}Tl in Normal Dogs

We studied four normal dogs during intravenous adenosine infusion without any surgical instrumentation in order to compare the normal file of stress SPECT ^{201}Tl and stress SPECT ^{99m}Tc-sestamibi (DuPont Nemours Co., Wilmington, DE). Since the major clinical uses of SPECT ^{99m}Tc-sestamibi and ^{201}Tl are for stress testing, we infused adenosine during injection of each

Received Jun. 24, 1992; revision accepted Sept. 30, 1992.

For correspondence or reprints contact: Robert L. Eisner, PhD, Carlyle Fraser Heart Center, Crawford Long Hospital of Emory University, Department of Nuclear Cardiology, 550 Peachtree St., Atlanta, GA 30365.

radionuclide. In a previous study, we found a dose of intravenously injected adenosine that produced reproducible maximal coronary vasodilation measured by an electromagnetic flow probe in dogs (*2*). Each dog was placed in the right decubitus position on the SPECT imaging table. Anesthesia was induced with 100 mg methohexital and maintained by inhalation of isoflurane (1.0%–2.0%). Adenosine was infused incrementally to achieve the doses (139 μg/kg/min) required to produce maximum vasodilation, i.e., peak stress. At peak stress, 5 mCi of ^{201}Tl was injected intravenously and the adenosine infusion was maintained for 3 min after injection and then stopped. Image acquisition for ^{201}Tl began within 5–10 min after cessation of stress. After the completion of the SPECT ^{201}Tl acquisition, the adenosine infusion was repeated for injection of ^{99m}Tc-sestamibi. At peak stress, ^{99m}Tc-sestamibi, range 30–35 mCi, was injected intravenously and the adenosine infusion was maintained for 3 min after injection and then stopped. SPECT ^{99m}Tc-sestamibi acquisition began 1–2 hr postinjection. An intravenous infusion of synthetic cholecystokinin (0.067 μg/min; Sincalide, Squibb Laboratories, Princeton, NJ) was maintained throughout the ^{99m}Tc-sestamibi SPECT acquisition to reduce gallbladder scatter contribution to images of the inferior wall of the heart. Cholecystokinin was started 50 min after ^{99m}Tc-sestamibi injection to avoid potential changes in myocardial distribution of ^{99m}Tc-sestamibi. At the conclusion of the ^{99m}Tc-sestamibi acquisition, the dogs were allowed to awaken and were returned to the kennel.

SPECT Acquisition Protocol

SPECT ^{99m}Tc-sestamibi and SPECT ^{201}Tl acquisition parameters were identical. A low-energy, high-resolution collimator (LEHR) was used to enhance SPECT resolution. View data were acquired on a General Electric 400AT/STAR SPECT system using a camera zoom factor of 1.6 into a 64 × 64 digital matrix (i.e., sampling size equaled 3.9 mm/pixel). Each dataset, consisting of 64 views, was acquired using a circular 180° anterior arc scan with a 45° RAO starting angle; time per view was 30 sec for a total acquisition time of 33.5 min.

Test of Degrading Effects of Attenuation and Resolution on SPECT ^{99m}Tc-Sestamibi Myocardial Perfusion Images

The influence of the variable view-to-view attenuation and resolution patterns on SPECT images is well demonstrated through a comparison of SPECT reconstructed body-fixed (transaxial) slices reconstructed from different 180° acquisition arcs. Thus, to test the degrading effects of resolution and attenuation on SPECT ^{99m}Tc-sestamibi image quality, a 360° SPECT acquisition was acquired in one dog. The same (transaxial) slice level was reconstructed for different 180° scans using the following starting positions and acquisition arcs: (a) 45° RAO starting position with an anterior arc, (b) Anterior starting position with an anterior arc, (c) Right lateral starting position with an anterior arc and (d) 45° RAO starting position with a posterior 180° scan (i.e., the 180° data from the 360° scan data set not normally used to produce the nominal SPECT reconstructed image). Maximum count circumferential profiles were used to compare the count distribution in SPECT transaxial images from the four scans.

Analysis of SPECT Images

The SPECT ^{201}Tl and ^{99m}Tc-sestamibi scans were processed identically and were assessed qualitatively and quantitatively through an extension of the authors' bull's-eye analysis software (*3,4*). After nine-point smoothing of the planar images, transaxial slices (3.9 mm thick) were reconstructed using ramp filtered back projection without attenuation correction. Following operator definition of the angularity of the heart in the thorax, vertical long-axis, horizontal long-axis and short-axis slices were derived from the transaxial data set. Following apical to basal short-axis slice selection by an experienced operator, ^{99m}Tc-sestamibi and ^{201}Tl short-axis slices were passed through the quantitative bull's-eye program where, using our new algorithm (*3,4*), the maximum count circumferential profiles for each short axis slice were coalesced into the two-dimensional bull's-eye representation. A normal bull's-eye file was generated from the individual bull's-eye arrays (*3*). The individual and normal bull's-eye displays were segmented into 10 regions, and count ratios between 9 different regions and a standardized region of the left ventricle were obtained. Comparisons of count ratios, ^{201}Tl versus ^{99m}Tc-sestamibi were performed by Student's t-test for paired data. Differences were considered significant when $p < 0.05$.

ECG-Gated Versus Ungated SPECT ^{99m}Tc-Sestamibi in Normal Dogs

We studied three additional normal dogs during adenosine infusion without any surgical instrumentation in order to construct a normal file of gated "stress" counts for comparison with ungated myocardial ^{99m}Tc-sestamibi activity. Along with the acquisition of the ungated SPECT study using the protocol described above, a two-frame gated SPECT study at diastole and systole was acquired similarly for approximately the same amount of time. In order to determine the appropriate imaging time for systole, the data were pooled from several (n = 25) previous imaging studies in which segmental shortening of regional myocardium had been recorded at various heart rates. In these previous studies, systole was defined as 20 msec before the peak negative left ventricular dP/dt and diastole as the initial upslope of dP/dt and left ventricular pressure (*5*). Generally, in normal animals the time of the shortest segmental length corresponds to systole, and the time of the longest length corresponds to diastole. Left ventricular pressures and ultrasonic crystals provide more specific markers than does the T-wave of the ECG as a marker for end-systole. From the pooled data and based on the heart rate of each dog, we calculated the average time from the R-wave to end-systole, and we calculated the maximum length of time that we could set the window for acquiring the diastolic and systolic images. Thus, diastolic images were acquired beginning at the R-wave and for a time interval of 50 msec, and systolic images were acquired at a time dependent on the dog's heart rate and with a 50 msec time interval. The SPECT ^{99m}Tc-sestamibi diastolic and systolic images were processed in an identical fashion to the ungated study. With bull's-eye arrays aligned at the apex, equal numbers of short axis slices were used to produce the diastolic and systolic bull's-eyes.

Relationship of SPECT ^{99m}Tc-Sestamibi Count Variations with Variations in Actual Left Ventricular Wall Thickness

Dual-Energy Acquisition of ^{201}Tl Point Source and SPECT ^{99m}Tc-Sestamibi Myocardial Perfusion Images to Align SPECT Short-Axis Slice and Pathological Slice. In one dog, a small 10 μCi ^{201}Tl point source was sutured to the epicardial surface of the left ventricle. At peak adenosine stress, 31 mCi of ^{99m}Tc-sestamibi was injected intravenously. Cholecystokinin was given to reduce

gallbladder activity. A dual energy, simultaneous ^{201}Tl and ^{99m}Tc-sestamibi SPECT scan was acquired over the nominal 180° anterior arc. Simultaneous SPECT reconstruction of the datasets from each isotope resulted in a series of ^{99m}Tc-sestamibi short axis slices along with a corresponding series of ^{201}Tl short-axis slices. The simultaneous processing produced identical alignment between the two sets of short-axis slices. The short-axis slice location of the ^{201}Tl point source was determined as the ^{201}Tl slice with maximum ^{201}Tl point source activity. A maximal count circumferential profile analysis with 40 radial vectors (9° angular intervals) was performed on the summed image resulting from the addition of the ^{201}Tl short-axis image and the ^{99m}Tc-sestamibi short axis slice image at the same short-axis slice level. The angular position of the point source was determined by comparison with the maximal count circumferential profile analysis performed on the same SPECT ^{99m}Tc-sestamibi short-axis slice without the ^{201}Tl point source.

Pathological Assessment of Myocardial Wall Thickness. After the SPECT scan, the animal was euthanized with a large dose of methohexital (100 mg) followed by potassium chloride (25 meq), and the heart was removed immediately. The atria, great vessels and right ventricle were removed and the isolated left ventricle was immersed in formalin. When fixed, the ventricle was sliced perpendicular to the long axis of its cavity at the position of the sutured ^{201}Tl point source. The slice was approximately 5 mm thick. Wall thickness was measured carefully (with calipers) on the apical and basal sides of 24 different angular locations. The apical and basal thickness values were averaged at each angle.

Comparison of Variation of Regional Myocardial Wall Thickness with the Variation of SPECT Reconstructed Counts. For comparison with the count profile (40 angular values), the 24 values of thickness were linearly interpolated to 40 values. A (relative) thickness value at each of the 40 angles was calculated as a percentage of the thickness value at the point source location. The (relative) thickness profile curve was normalized to have the same area as the (relative) count profile curve where each value was calculated as a percentage of the counts at the point source location. A chi-square analysis was used to compare the relative thickness (expected) versus relative count (observed) profile curves.

RESULTS

Comparison of SPECT Reconstructed ^{99m}Tc-Sestamibi Images with ^{201}Tl Images from Normal Dogs

The SPECT ^{99m}Tc-sestamibi and ^{201}Tl bull's-eye displays from the normal file comprised of four normal animals are shown in Figures 1A and 1B. Count ratios between nine different bull's-eye regions and a tenth region with the largest number of counts (right-side of bull's-eye in each case) are shown in Figures 1C and 1D. Decreased counts at the apex (count ratio = 0.68 with respect to the hottest segment for both SPECT studies) extending into the anterior segment (with respect to the hottest segment the mid-ventricular (slices 4–12) count ratio = 0.81 for

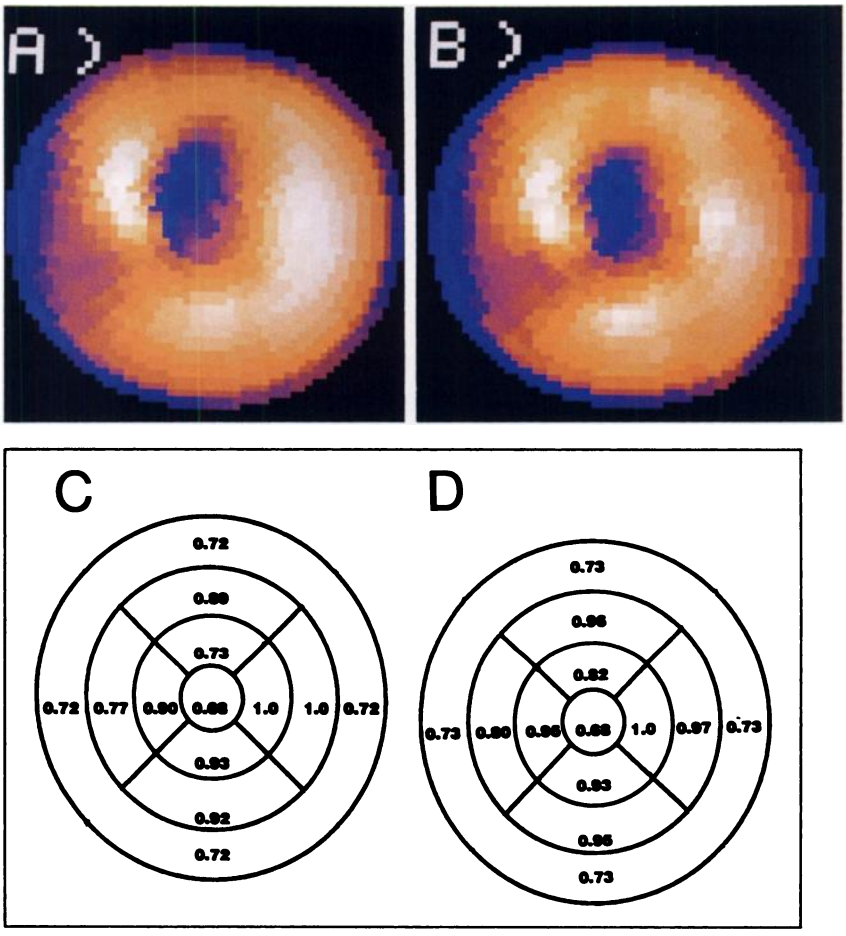

FIGURE 1. Comparison of pooled SPECT ^{99m}Tc-sestamibi and SPECT ^{201}Tl bull's-eye displays from the normal file comprised of four normal dogs. (A) SPECT ^{99m}Tc-sestamibi. (B) SPECT ^{201}Tl. (C) SPECT ^{99m}Tc-sestamibi. Count ratios are shown relative to the region of the bull's-eye with most counts. (D) SPECT ^{201}Tl. Count ratios are shown relative to the region of the bull's-eye with most counts. The bull's-eye display consists of 15 slices from apex (center) to base (periphery). Counts are color-coded with white = maximum and blue = 70% of maximum. Figures 1C,D show relative count ratios for the mid-ventricular region (slices 5–8; slices 9–12; four 90° wedges), apical region (slices 1–4) and one basal region (slices 13–15). SPECT ^{201}Tl and ^{99m}Tc-sestamibi bull's-eye displays are very similar in normal dogs.

SPECT ^{99m}Tc-sestamibi and 0.90 for SPECT ^{201}Tl), and a hot right side versus left side (left side to right side mid-ventricular count ratio = 0.84 for SPECT ^{99m}Tc-sestamibi versus 0.89 for SPECT ^{201}Tl) are the dominant features of the bull's-eye displays shown in Figure 1. Qualitative examination of the color bull's-eyes (Fig. 1A,1B) and the corresponding regional count ratios (Fig. 1C,1D) shows that the two perfusion agents as imaged by SPECT in normal dogs are very similar. Results of paired t-tests showed no significant differences in count ratios in eight of nine regions demonstrating that SPECT ^{201}Tl and SPECT

^{99m}Tc-sestamibi images are virtually identical in normal dogs.

Attenuation and Resolution Effects on SPECT ^{99m}Tc-Sestamibi Images

Reconstructed ^{99m}Tc-sestamibi transaxial images at the same slice level from different 180° acquisition arcs from a 360° SPECT acquisition of one normal dog are shown in Figure 2A. Figure 2B shows the maximal count profiles obtained from these slice data. As expected from the degrading effects of resolution and attenuation, the transaxial images show regional count variations which depend on the starting angle and the 180° SPECT acquisition arc. Depending on the anterior arc, lateral-to-septal wall count ratios vary by 20% while "apical"-to-septal wall count ratios vary by 15%. Note that count values in the lateral wall are depressed significantly in the image reconstructed from an anterior arc scan with an anterior starting angle (upper right-Fig. 2A). Also, the angular position of the hot spot on the septal wall at the junction of the right and left ventricles depends on the acquisition arc and starting angle.

The absolute number of counts and the shape of the count profile distribution from the posterior 180° acquisition arc differ significantly from those obtained from all anterior arc scans. The distorted image data from the posterior 180° acquisition result from the variable view-to-view attenuation pattern which differs markedly from the corresponding pattern of the 180° anterior arc scan. The significant difference in SPECT image quality between the anterior and the severely distorted posterior scans argues strongly against using the ^{99m}Tc posterior arc dataset by itself or as a component of a 360° SPECT acquisition. Accordingly, this result suggests that like SPECT ^{201}Tl, SPECT ^{99m}Tc-sestamibi should be acquired with a 180° anterior arc scan (*1,6–8*).

Gated and Ungated SPECT ^{99m}Tc-Sestamibi Images from Normal Dogs

The gated and ungated SPECT ^{99m}Tc-sestamibi color bull's-eye displays, and regional count ratios, are shown in Figure 3 for the pooled (n = 3) data. The ^{99m}Tc-sestamibi bull's-eye displays are not homogeneous; they all exhibit similar features with a decrease of counts at the center ("apex") and a "hot" right side, (the average right-side to

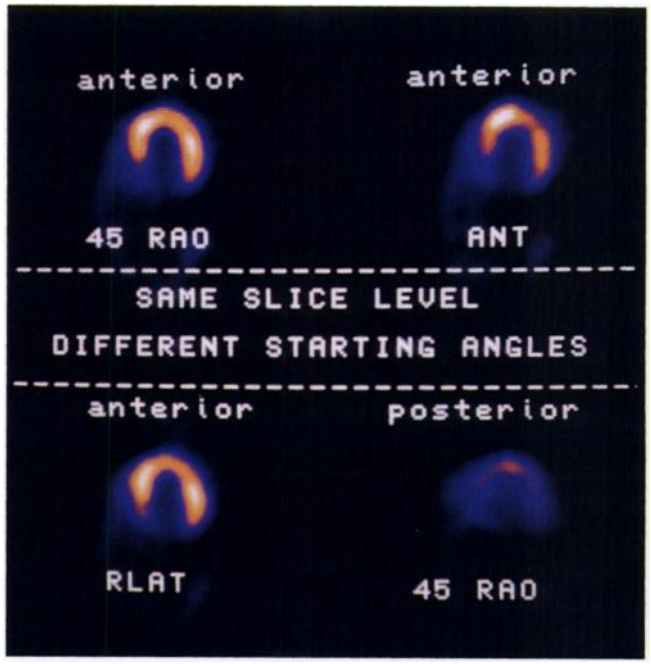

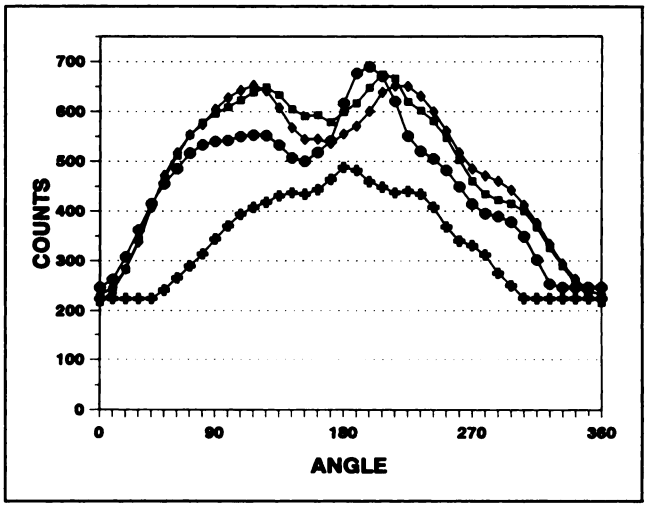

FIGURE 2. Effect of different 180° acquisition arcs on SPECT ^{99m}Tc-sestamibi image quality. The label above each image describes the 180° acquisition arc, and the label below describes the starting angle. Images have the lateral wall on the right and the septal wall on the left. (Top) Transaxial images with different starting angles and different acquisition arcs (anterior and posterior). RAO = right anterior oblique; ANT = anterior; RLAT = right lateral. (Bottom) Quantitative maximal count circumferential profiles from the images shown in Figure 2A. ♦ = RAO starting angle and anterior arc scan, ■ = RLAT starting angle and anterior arc scan, ● = ANT starting angle and anterior arc scan, + = RAO starting angle and posterior arc scan. Relative counts in the lateral wall [peak in profile curve between 90° and 180°] and the angular position and count activity of the hot spot on the ventricular septum (peak in profile curve between 180° and 270°) depend on the 180° acquisition arc. Differences in the image count profiles are due to the inability of the SPECT reconstruction program to compensate for the variable effects of attenuation and resolution in the projection view data.

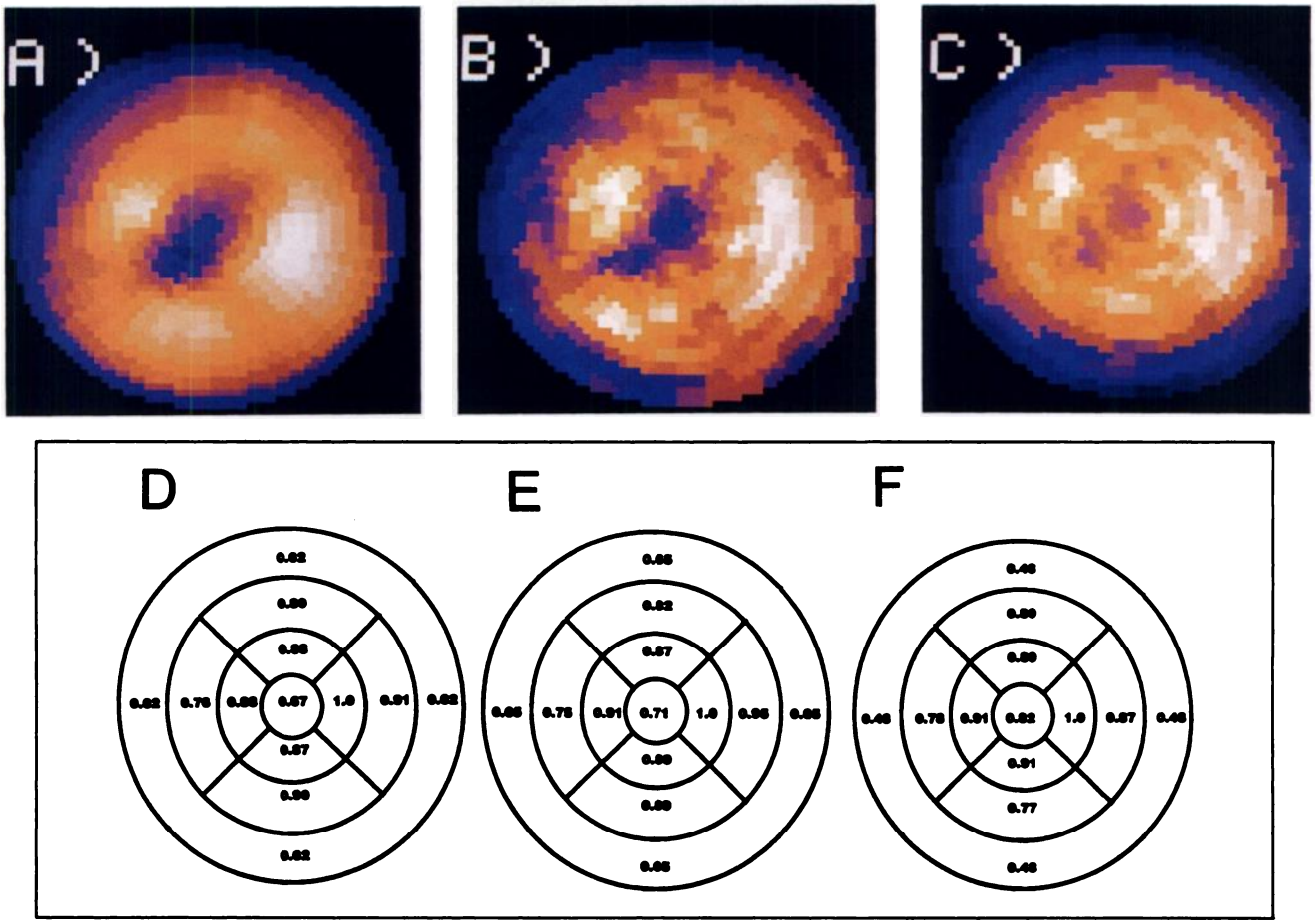

FIGURE 3. (A) Ungated SPECT ^{99m}Tc-sestamibi bull's-eye display pooled from three normal dogs. (B) Diastolic SPECT ^{99m}Tc-sestamibi bull's-eye display for the same animals shown in A. (C) Systolic SPECT ^{99m}Tc-sestamibi bull's-eye display for the same animals shown in A. (D) Count ratios from the ungated ^{99m}Tc-sestamibi bull's-eye. (E) Count ratios from the diastolic ^{99m}Tc-sestamibi bull's-eye. (F) Count ratios from the systolic ^{99m}Tc-sestamibi bull's-eye. The ungated and gated bull's-eyes show similar distortions with a cold apex and a hot right side.

left-side count ratio = 1.17 (ungated), 1.17 (diastolic), 1.10 (systolic)). The small hot area at about "10 o'clock" in the mid-ventricular region of each bull's-eye display corresponds anatomically to the junction of the left and right ventricles. The large decrease of counts in the basal section of the systolic bull's-eye is a reflection of the decreased apical to basal length of the left ventricle at systole versus diastole. The enhancement of the count ratio in the apical sector at systole (0.82; Fig. 3F) versus diastole (0.71; Fig. 3E) is most likely a partial volume effect; the enhanced thickness of the LV, in conjunction with a decrease in left ventricular cavity size at systole, results in systolic images which have significant blurring of counts between the myocardial walls to yield enhanced counts in the systolic versus the better delineated diastolic apical region.

Relationship of SPECT ^{99m}Tc-Sestamibi Count Profiles with Myocardial Wall Thickness Variations

The relative count profile curve (filled rectangles) from the reconstructed SPECT ^{99m}Tc-sestamibi short axis slice compared to the corresponding thickness profile curve (filled circles) from the excised heart slice, following registration at the ^{201}Tl point source location, is shown in Figure 4. Chi-square analysis showed no similarity between relative SPECT counts and actual measured wall thickness (χ^2/(degree of freedom) = 1.85; $p < 0.001$).

DISCUSSION

In agreement with the predictions of our computer simulation model (*1*) SPECT ^{99m}Tc-sestamibi myocardial perfusion images in dogs show:

1. Differences in regional count distributions which depend on the exact starting angle and 180° acquisition arc used for SPECT reconstruction.
2. Severe distortions with posterior 180° acquisition.
3. Distortions equivalent to SPECT ^{201}Tl as reflected by the similarity of the SPECT ^{201}Tl and SPECT ^{99m}Tc-sestamibi bull's-eye displays.

The agreement between the computer model predictions (*1*) and the animal data presented here suggests strongly

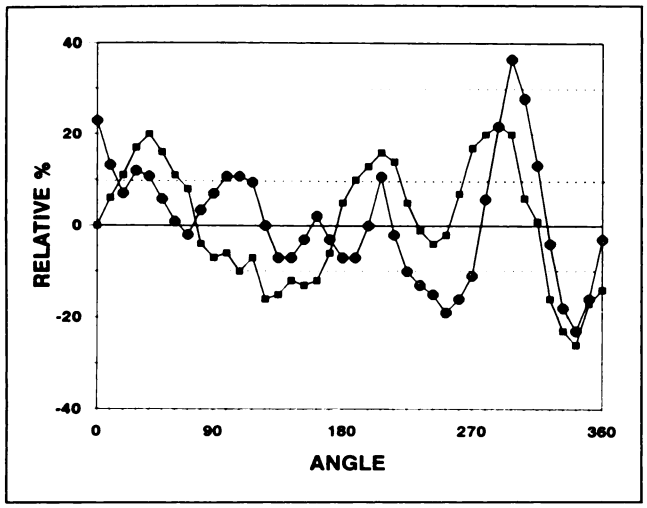

FIGURE 4. Comparison of relative count profile curve (filled rectangles) from a SPECT short-axis slice and relative myocardial wall thickness profile (filled circles). SPECT count distribution is not similar to the myocardial wall thickness distribution ($p < 0.001$).

that the inhomogeneity in SPECT ^{99m}Tc-sestamibi images is due mainly to the degrading effects of attenuation and resolution which are not compensated for in the SPECT reconstruction process. The count density distortions in the ungated ^{99m}Tc-sestamibi scans cannot be related to cardiac motion since we find equivalent inhomogeneity in the gated and ungated scans. The count distortions cannot be due to differential deposition of isotope since previous dog experiments with microspheres have shown that blood flow has random variability but no systematic differences among anatomically different areas of the myocardium (*9*). While we have not found any similarity between actual wall thickness and SPECT reconstructed counts, it seems reasonable to associate some degree of count heterogeneity to variations in myocardial wall thickness (*10*). The results of this animal study in conjunction with the computer simulation predictions suggest that decreased counts at the LV "apex" and the asymmetry in left-right counts in SPECT ^{99m}Tc-sestamibi and SPECT ^{201}Tl bull's-eyes in normal dogs (Figs. 1 and 2) can be attributed to the lack of compensation for attenuation and resolution during the SPECT imaging and reconstruction process in addition to any anatomical variability in myocardial wall thickness (e.g., apical thinning).

We have previously reported that stress SPECT ^{201}Tl bull's-eye displays in our patient normal files show a hot lateral wall compared to the septum for both males (n = 50; average lateral-to-septal wall count ratio = 1.16 in the mid-ventricular region) and females (n = 50; average lateral-to-septal wall count ratio = 1.11 in the mid-ventricular region) (*4*). A similar effect is reported here in the SPECT ^{201}Tl dog bull's-eye (average right-side to left-side count ratio = 1.12) and in the SPECT ^{99m}Tc-sestamibi bull's-eye (count ratio = 1.19). We have been careful to designate the segment of the dog bull's-eye as "right" or "left" since—in contrast to the human studies—the "right-side" of the dog bull's-eye corresponds to portions of the anterior and anterolateral wall (not lateral, as in humans) and the "left-side" to the inferoseptal and inferior wall (not septal, as in humans) of the dog left ventricle. The distinction is important since it is then the body-fixed slices which show similar count density distortions in humans and dogs. In conjunction with our simulation model prediction, and with the animal findings of a right-to-left bull's-eye count asymmetry, it seems reasonable to attribute the count density distortions in the male and female (human) SPECT ^{201}Tl bull's-eye to an artifact of the SPECT imaging process (i.e., no compensation for the effects of resolution and attenuation degradation), and not to physiological or anatomical variability. In this regard, Yamashita, et al. (*11*) have reported an increased ratio of septal-to-lateral wall counts in ECG-gated, attenuation-corrected, N^{13}-NH_3 PET scans at diastole, with no significant count variation at systole, in nine normal male volunteers. Grover-McKay, et al. (*12*) reported a septal-to-lateral count ratio of 0.98 ± 0.07 in 10 normal subjects in ungated N^{13}ammonia. Schwaiger and Muzik (*13*) reported a septal-to-lateral count ratio of 1.0 in 15 normal subjects (8 male, 7 female) in ungated ^{82}Rb. Thus, the asymmetry in wall counts in PET, using a myocardial perfusion imaging agent (N^{13}-NH_3 or ^{82}Rb) similar to ^{201}Tl, differs from that found in our SPECT ^{201}Tl studies in humans, i.e., increased ratio of lateral-to-septal counts. In contrast to SPECT, PET compensates for attenuation and has better system resolution; as such, it should provide a less distorted representation of the true myocardial count distribution as modified by myocardial wall thickness and blood flow variability. Thus, the difference in myocardial perfusion distributions between SPECT ^{201}Tl and the more accurate PET in normal subjects further supports our conclusion that the variations in SPECT counts do not have an anatomical or physiological basis. Finally, the similarity in count inhomogeneity of the SPECT ^{99m}Tc-sestamibi and SPECT ^{201}Tl bull's-eye displays in dogs (Fig. 1) further suggests that we should not expect any major improvement in SPECT ^{99m}Tc-sestamibi image quality (i.e., significantly less count density distortion) in humans from the differences in the view-to-view attenuation/scatter/resolution contributions of ^{99m}Tc versus ^{201}Tl.

ACKNOWLEDGMENT

Supported by an American Heart Association/Georgia Affiliate Grant-in aid.

REFERENCES

1. Eisner RL, Nowak DJ, Pettigrew RI, Fajman W. Fundamentals of 180° acquisition and processing in SPECT imaging. *J Nucl Med* 1986;17:1717–1728.
2. Leon AR, Eisner RL, Martin SE, et al. Comparison of SPECT thallium-201 and SPECT Tc^{99m}-sestamibi myocardial perfusion imaging in dogs. *J Am Coll Cardiol* 1992:in press.

3. Eisner RL, Tamas MJ, Cloninger K, et al. Normal SPECT thallium-201 bull's-eye display: gender differences. *J Nucl Med* 1988;29:1901–1909.
4. Boyers AS, Eisner RL, Chu TH, Oates J, Curien B, Patterson RE. Quantitative analysis of myocardial perfusion scans with 3-D display [Abstract]. *J Nucl Med* 1990;31:808.
5. Vatner SF. Correlation between acute reduction in blood flow and function in conscious dogs. *Circ Res* 1980;47:201–207.
6. Ritchie JL, Olson DO, Williams DL, et al. Transaxial computed tomography with Tl-201 in patients with prior myocardial infarction [Abstract]. *J Nucl Med* 1981;22:P11.
7. Besozzi MC, Rizz HR, Rogers EL, et al. Rotating gamma camera ECT of Tl-201 in the human heart [Abstract]. *J Nucl Med* 1981;22:P11.
8. Tamaki N, Mukai T, Ishii Y, et al. Comparative study of thallium emission myocardial tomography with 180 degree and 360 degree data collection. *J Nucl Med* 1982;23:661–666.
9. Cobb FR, Bache RJ, Greenfield JC. Regional myocardial blood flow in awake dogs. *J Clin Invest* 1974;53:1618–1626.
10. Hoffman EJ, Huang SC, Phelps ME. Quantitation in positron emission computed tomography: 1. Effect of object size. *J Comput Assist Tomography* 1979;3:299–308.
11. Yamashita K, Tamaki N, Yonekura Y, et al. Quantitative analysis of regional wall motion by gated myocardial positron emission tomography: validation and comparison with left ventriculography. *J Nucl Med* 1989;30:1775–1786.
12. Grover-McKay M, Schwaiger M, Krivokapich J, Perloff JK, Phelps ME, Schelbert HR. Regional myocardial blood flow and metabolism at rest in mildly symptomatic patients with hypertrophic cardiomyopathy. *J Am Coll Cardiol* 1989;13:317–324.
13. Schwaiger M, Muzik O. Assessment of myocardial perfusion by positron emission tomography. *Am J Cardiol* 1991;67:35D–43D.

(continued from page 233)

SELF-STUDY TEST
Pulmonary Nuclear Medicine

ANSWERS

these changes, indeed, may have occurred. The examination should be considered nondiagnostic up to this point. A new chest radiographic examination should be obtained (ideally, standard erect posteroanterior and lateral films). If matching infiltrates have developed, the findings would indicate an intermediate probabilty of pulmonary embolism; if not, a high probability interpretation would be appropriate. As a corollary, it should be noted that an increasing period of time between onset of symptoms and ventilation perfusion imaging is associated with an increasing likelihood that an intermediate-probability interpretation will result, in part reflecting the evolution of new radiographic abnormalities in patients with pulmonary embolism.

The use of the term "ventilationperfusion match" can be misleading. A ventilation-perfusion match only represents a low probability for pulmonary embolism when the chest radiograph is normal. A radiographic opacity correlating with a perfusion defect takes precedence over a ventilation perfusion match, and should lead to an intermediate-probability interpretation.

References

1. Alderson PO, Biello DR, Sachariah G, Siegel BA. Scintigraphic detection of pulmonary embolism in patients with obstructive pulmonary disease. *Radiology* 1981;138:661-666.
2. Biello DR, Mattar AG, Osei-Wusu A, Alderson PO, McNeil BJ, Siegel BA. Interpretation of indeterminate lung scintigrams. *Radiology* 1979; 133:189-194.
3. Davis RB, Schauwecker DS, Siddiqui AR, et al. Indeterminate lung imaging. Can the number be reduced? *Clin Nucl Med* 1986;11:577-582.
4. Rosen JM, Pallestro CJ, Markowitz D, Alderson PO. Significance of single VP mismatches found in Kr-81m/Tc-99m lung scans. *J Nucl Med* 1986;27:361-365.

Items 6-10: Assessing the Post-Test Probability of Pulmonary Embolism

Answers: 6, C; 7, D; 8, D; 9, C; 10, C

The principles of Bayes' theorem can be used to answer these questions, which require that one consider both the scintigraphic findings and the clinical data for each patient. Although ventilation-perfusion scintigrams usually are interpreted with reference to the likelihood or probability of pulmonary embolism corresponding to a particular set of findings on the images, the actual post-test probability of embolism in any patient depends on both the scintigraphic result and the pretest probability of pulmonary embolism based on the constellation of risk factors, symptoms, physical signs, laboratory data, and radiographic findings in a particular patient. Admittedly, this probability is difficult to determine precisely, but experienced clinicians can estimate the likelihood of embolism as low, moderate, or high with reasonable accuracy by carefully evaluating all of the patient's clinical information. The first patient has intermediate probability scintigraphic findings, but a very high clinical probability for pulmonary embolism. Thus, she has a moderately high post-test probability of embolism. Some clinicians might consider anticoagulation at this point, but most others would proceed with further diagnostic studies in this clinical setting.

The history and radiographic findings in the second patient are most suggestive of heart disease with congestive failure, not pulmonary embolism. Thus, the post-test probability of embolism is low, and in this setting, many physicians would not search further for pulmonary embolism despite the intermediate-probability scintigraphic result. Additionally, one recent study has suggested that a perfusion defect corresponding to a pleural effusion is unlikely to represent pulmonary embolism. However, there is not general agreement on this point, and most diagnostic schemes still classify such findings as indicative of an intermediate likelihood for pulmonary embolism on scintigraphic grounds alone.

There is no reason for the third patient to have acute pulmonary embolism. This single perfusion defect, leading to an intermediate-probability scintigraphic interpretation, is likely due to one of the other causes discussed in the syllabus text.

The fourth patient, who is on chronic hemodialysis, has a high-probability scintigraphic result. Because pulmonary embolism is relatively uncommon in patients on hemodialysis, presumably because they receive heparin during dialysis and because of the hemostatic defect associated with renal insufficiency, the pre-test likelihood of embolism is low, leading to only a moderate post-test probability of embolism. Thus, it would seem prudent to do further testing, such as pulmonary angiography or a search for lower-extremity deep venous thrombosis, in this patient.

The last patient has a very suggestive history for pulmonary embolism but an apparently low-probability scintigraphic study. Thus, the post-test probability of embolism is moderate. In fact, there is an additional clue that pulmonary emboli may be present: the defects are wedge-shaped and segmental and the symptoms began a very short time before the lung scan. Infrequently, pulmonary emboli may lead to reflex bronchoconstriction during the first few hours after the embolic event. This bronchoconstriction is likely due to local hypocapnia and the release of serotonin and other substances from platelets at the site of the embolus. The associated abnormality on ventilation imaging will closely match the perfusion defect and will generally resolve within approximately 6 hours of the time of embolization. Recognition of this phenomenon can be very difficult because ventilation perfusion matches with a normal radiograph generally are interpreted as indicating a low-probability for pulmonary embolism. The principal features of this case suggesting pulmonary embolism with bronchospasm are

(continued on page 296)